university of groningen

University Medical Center Groningen

University of Groningen

Antiferromagnetic Ordering and Uncoupled Spins in CaFe2O4 Thin Films Probed by Spin Hall Magnetoresistance

Damerio, Silvia; Kaverzin, Alexey A.; Ocelík, Václav; Hoogeboom, Geert R.; van Wees, Bart J.; Noheda, Beatriz

Published in:
Advanced electronic materials

DOI:
10.1002/aelm.202100963

IMPORTANT NOTE: You are advised to consult the publisher's version (publisher's PDF) if you wish to cite from it. Please check the document version below.

Document Version
Publisher's PDF, also known as Version of record

Publication date:
2022

Link to publication in University of Groningen/UMCG research database

Citation for published version (APA):
Damerio, S., Kaverzin, A. A., Ocelík, V., Hoogeboom, G. R., van Wees, B. J., & Noheda, B. (2022). Antiferromagnetic Ordering and Uncoupled Spins in $CaFe_2O_4$ Thin Films Probed by Spin Hall Magnetoresistance. *Advanced electronic materials*, *8*(6), [2100963]. https://doi.org/10.1002/aelm.202100963

Copyright
Other than for strictly personal use, it is not permitted to download or to forward/distribute the text or part of it without the consent of the author(s) and/or copyright holder(s), unless the work is under an open content license (like Creative Commons).

The publication may also be distributed here under the terms of Article 25fa of the Dutch Copyright Act, indicated by the "Taverne" license. More information can be found on the University of Groningen website: https://www.rug.nl/library/open-access/self-archiving-pure/taverne-amendment.

Take-down policy
If you believe that this document breaches copyright please contact us providing details, and we will remove access to the work immediately and investigate your claim.

Downloaded from the University of Groningen/UMCG research database (Pure): http://www.rug.nl/research/portal. For technical reasons the number of authors shown on this cover page is limited to 10 maximum.

Check for updates

ADVANCED ELECTRONIC MATERIALS
www.advelectronicmat.de

Antiferromagnetic Ordering and Uncoupled Spins in $CaFe_2O_4$ Thin Films Probed by Spin Hall Magnetoresistance

*Silvia Damerio, Alexey A. Kaverzin, Václav Ocelík, Geert R. Hoogeboom, Bart J. van Wees, and Beatriz Noheda**

$CaFe_2O_4$ is a uniaxial antiferromagnet displaying two coexisting magnetic orderings, A and B, characterized by ↑↑↓↓ and ↑↓↑↓ spin modulation, respectively, and the emergence of a net magnetization in a limited temperature range, which is not yet understood. The spin Hall magnetoresistance (SMR) is probed at the interface between *Pt* and $CaFe_2O_4$ and the crystallographic domain structure of thin film samples is exploited to perform single- and multi-domain scale measurements. The SMR response, upon rotating the magnetic field along three orthogonal planes, shows little effect of the strong magnetocrystalline and shape anisotropies. Together with the response to a varying magnetic field strength, the modulations in the SMR signal allow to extract two contributions: one corresponds to the long-range antiferromagnetic ordering, supporting a single ground state scenario; while the second contribution originates from uncompensated, non-interacting spins. These are expected to exist at the antiphase boundaries between antiferromagnetic domains. Here, it is shown that these are also uncoupled from the antiferromagnetic ordering. Nonetheless, the long range correlations that emerge in the proximity of the critical antiferromagnetic transition can give rise to ordering of the uncompensated spins and be responsible for the net magnetization observed in this antiferromagnet.

1. Introduction

The use of antiferromagnetic (AF) materials as active elements in devices is increasingly attracting interest, as it offers the possibility for complex functionalities.[1] This is made possible by the availability of a wide variety of different AF structures arising from the interplay of exchange interactions between spins with multiple strengths (J). In addition, antiferromagnets can display strong magnetoelastic coupling, insulating behavior, zero stray fields and THz dynamics, which all make them promising candidates for the next generations of spin-based technologies.[2–4] The absence of net magnetization in these materials brings the need to control and probe the AF state using indirect methods, such as via electrical manipulation and reading of the spin texture.[5–8] Recently, this has been implemented in spintronic devices via the interconversion of a charge current into a spin current at the interface between a heavy metal (HM) and a magnetic insulator (MI) by means of the spin Hall magnetoresistance (SMR) effect.[9] SMR measurements are not only the first step to assess the possibility of spin injection in AF insulators, but also a powerful tool to characterize the magnetic structure of the material as they give access to the local spin structure, differently from most other techniques.[10–15]

In this paper we report the use of SMR measurements in order to characterize the antiferromagnetic oxide $CaFe_2O_4$. This material crystallizes in an orthorhombic lattice with the *Pnma* space group. In this structure, the Fe^{3+} ions are arranged in a honeycomb pattern and form zig-zag chains running along the *b*-axis, which is the magnetic easy axis. Oxygen atoms in octahedral coordination connect the Fe^{3+} spins and mediate the magnetic super-exchange interaction. Intra-chain FeO_6 octahedra share corners, leading to strong antiferromagnetic coupling (J_3 and J_4), while the inter-chain connection, through edges, is weaker (J_1 and J_2) and close to the cross-over between positive and negative.[16] This leads to the observation of two competing magnetic structures, termed A and B, that differ in their the *c*-axis stacking of spin chains; ↑↓↑↓ (B phase) and ↑↑↓↓ (A phase).[17] Although the first report on the magnetic structure of $CaFe_2O_4$ dates back to the 1960s,[18] different mechanisms for the A/B coexistence have been proposed, with some authors showing coexistence of both A and B down to low temperature,[17,19] while others found coexistence only close to the Néel Temperature (T_N) of approximately 200 K.[20] In addition,

S. Damerio, A. A. Kaverzin, V. Ocelík, G. R. Hoogeboom, B. J. van Wees, B. Noheda
Zernike Institute for Advanced Materials
University of Groningen
Groningen 9747 AG, The Netherlands
E-mail: b.noheda@rug.nl

B. Noheda
Groningen Cognitive Systems and Materials Center (CogniGron)
Groningen 9747 AG, The Netherlands

The ORCID identification number(s) for the author(s) of this article can be found under https://doi.org/10.1002/aelm.202100963.

© 2021 The Authors. Advanced Electronic Materials published by Wiley-VCH GmbH. This is an open access article under the terms of the Creative Commons Attribution-NonCommercial License, which permits use, distribution and reproduction in any medium, provided the original work is properly cited and is not used for commercial purposes.

The copyright line for this article was changed on 20 December 2021 after original online publication.

DOI: 10.1002/aelm.202100963

a net spontaneous magnetization, whose origin is still under debate, has been measured in $CaFe_2O_4$ crystals, ceramics and thin films, peaking at around 120 K.[19,21] The discrepancies in the observed magnetic behaviour have been attributed to different degrees of strain in different samples.[22] In a recent work[21] we have synthesized epitaxial $CaFe_2O_4$ thin films for the first time. These films show many of the puzzling features previously reported for single crystals, such as net magnetization, but display a single phase transition (see Supporting Information). In addition, the films reveal a unique domain structure, which raises questions about the contribution of domain walls to the magnetic responses. Therefore, complementing previous results with magnetic data on thin film samples could help to clarify the nature of the ordering in this material.

In this work, the combination of transport measurements with an in-depth study of the crystal structure of the films by means of electron back-scatter diffraction (EBSD) allows to probe the ferromagnetic and antiferromagnetic response locally for each structural domain and globally for multi-domain devices. The experiments reveal emergent behavior that cannot be trivially explained by a purely antiferromagnetic spin configuration nor by the domain structure of the samples and support the hypothesis of the presence of a field induced magnetization in addition to a single antiferromagnetic ground state.

1.1. Introduction to the Spin Hall Magnetoresistance

In SMR measurements, an in-plane charge current in the HM generates a perpendicular spin current via the spin Hall effect (SHE) that, in turn, leads to a spin accumulation at the interface between the HM and the MI. If the direction of the magnetic moments in the MI has a component perpendicular to the spin-polarization of the spins, the spin current is partially absorbed through the spin transfer torque, leading to a high longitudinal resistance state in the HM. On the other hand, if the magnetic moments are collinear with the accumulated spin-polarization, the spin current is reflected at the NM/MI interface and converted into an additional charge current via the inverse spin Hall effect, yielding a state of lower longitudinal resistance in the HM.[23]

By now it is well established[9,15,24] that the SMR provides unique information about the magnetic state of (anti-)ferromagnets near the interface with the heavy metal. For in-plane magnetic field rotation, the FM response (positive SMR amplitude) is out of phase with respect to the AF one (negative SMR amplitude). In the case of a ferromagnet, the magnetization ($\vec{M}$) aligns with the magnetic field ($\vec{H}$), leading to a $cos^2(\alpha)$ modulation of the longitudinal resistance (R_L), with α being the angle between the directions of $\vec{H}$ and the current (i). The resistance is, therefore, maximum when the spins are parallel to the current direction ($\alpha = 0°$, which defines positive SMR). In transverse geometry, the resistance follows a $sin(\alpha)cos(\alpha)$ modulation,[25] which is 45° shifted with respect to the longitudinal one.

On the other hand, when a magnetic field is applied to a uniaxial antiferromagnet, different mechanisms can influence its magnetic order, depending on the field direction and amplitude compared to the magnetic anisotropy and exchange interactions. If a large enough magnetic field is applied along the easy axis, a spin-flop transition occurs,[3] which results in an orientation of the Néel vector ($\vec{L}$) of the AF ordering perpendicular to the field direction. Rotating the magnetic field can then have two effects: either it induces a rotation of $\vec{L}$ in the individual AF domains along with $\vec{H}$ and, in the presence of multiple energetically equivalent magnetic domains, it breaks their degeneracy and creates a force that pushes the domain walls toward the less stable domains. In both cases, the angular dependent magnetoresistance (ADMR) would show a 90° phase shift with respect to prototypical YIG/Pt (ferrimagnetic) bilayers, giving rise to a negative amplitude. This negative SMR has been observed in easy-plane antiferromagnets such as NiO[26,27] and $\alpha - Fe_2O_3$[28] and also in ferrimagnets close to the compensation temperature, where the spin-flop transition is possible at lower magnetic fields.[29–32]

In addition, in an antiferromagnet, a tilt of the spins constituting the two magnetic sublattices in the direction of the field can also occur, inducing a net magnetization that affects the SMR response.[3] If the magnitude of such tilt is larger than 45° from the spin-flop direction, then this contribution will dominate and will give rise to an overall positive amplitude of the SMR. Therefore, the in-plane ADMR is a combination of these two out-of-phase responses. On the other hand, the expected behaviour for pure FM and AF ordering is different when the magnetic field is rotated in the planes normal to the sample surface. In particular, when the field rotates within the plane containing the current direction ($n - i$), a $\vec{M}$ rotating coherently with $\vec{H}$ is always perpendicular to the spin accumulation and thus no longitudinal resistance modulation is observed for pure FM ordering. On the other hand, a modulation can be expected in an antiferromagnet with the easy axis parallel to the current direction. In this case, R_L is highest when $\vec{H}$ is perpendicular to the surface and lowest when it is parallel to i, pushing $\vec{L}$ from $\vec{i}$ to $\vec{t}$. Interestingly, the amplitude of the modulation here decreases with increasing applied field as the component of $\vec{L}$ parallel to the spin accumulation direction decreases in the low resistance state. With a similar argument, when $\vec{H}$ rotates within the plane perpendicular to the current direction ($n - t$), $\vec{L}$ aligns always perpendicular to the spin accumulation because of the easy axis direction. Therefore, a modulation of R_L in this plane cannot arise from the spin-flop state and indicates the presence of a magnetization. Therefore, for a complete picture of the contributions playing a role in the ADMR for a complex material like $CaFe_2O_4$, the response needs to be studied in all three orientations.

2. Sample Preparation and Measurement Technique

The $CaFe_2O_4$ thin film samples used in this study were grown by pulsed laser deposition on TiO_2 (110) substrates, as reported in Ref. [21]. Previous characterization by means of X-ray diffraction revealed the presence of multiple structural domains with different in-plane and out-of-plane orientations, induced by the underlying template and the self-grown $CaTiO_3$ buffer layer.[21] The different structural domains are themselves made of needle-like crystals growing along the magnetic easy axis direction. This is clearly visible with atomic force microscopy (AFM), as shown in **Figure 1**a.

In-depth characterization of the domain structure of $CaFe_2O_4$ has been achieved by means of Electron Backscatter Diffraction (EBSD) in a Scanning Electron Microscope. As depicted in

© 2021 The Authors. Advanced Electronic Materials published by Wiley-VCH GmbH

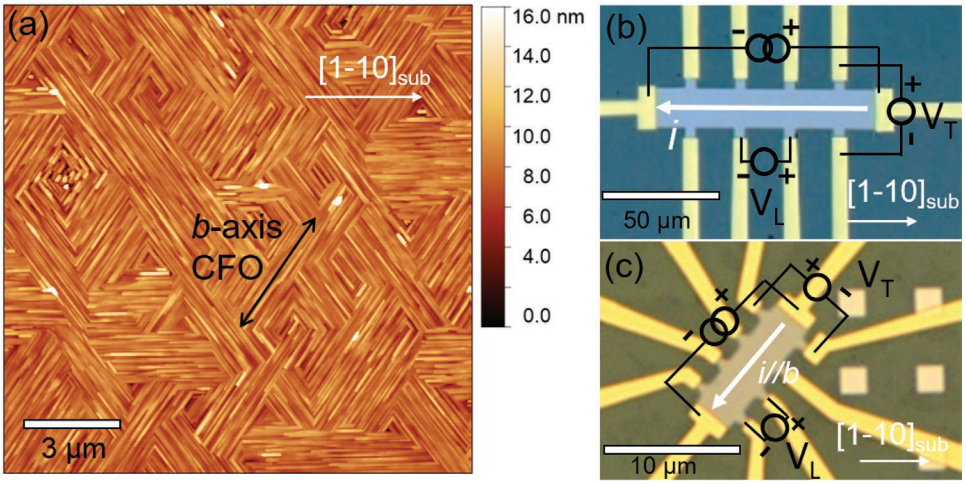

Figure 1. Samples and devices. a) AFM topography of a 84 nm thick $CaFe_2O_4$ thin film. Optical microscope images showing b) a large (100 μm) Hall-bar device covering multiple domains and c) a small (10 μm) Hall-bar device on a single structural domain. The direction of the substrate's $[1\bar{1}0]$ edge is indicated to show the relative orientation of the devices and a schematic of the electrical connections is included.

Figure 2a, nine different domain types are found. Three of them display the same (001) out-of-plane direction but differ in the in-plane. In domain *T*1 the ⟨010⟩ direction is parallel to the [100] sample axis (substrate $[1\bar{1}0]$). In *T*2 and *T*3 ⟨010⟩ is parallel to $[5\bar{7}0]$ and [570], respectively. This corresponds to a ±55° rotation with respect to *T*1. The remaining six domain types display (302) out-of-plane direction. For these domains, the same three in-plane orientations are also found (*T*4*a*, *T*5*a* and *T*6*a*). In addition, a rotation of 180° along the out-of-plane direction of the unit cell generates a twin variant of each domain type (*T*4*b*, *T*5*b* and *T*6*b*). The same rotation applied to domains *T*1, *T*2 and *T*3 does not lead to a different crystallographic orientation as it coincides with a rotation around the crystallographic axis ⟨001⟩. A schematic representation of the unit cell spatial orientation of the various domains is visible in Figure 2b as axonometric projections (top view), superimposed on the correspondent SEM image. The data from the same EBSD scan is also reproduced in the maps of Figure 2c,d where only the out-of-plane and in-plane directions of the domains are shown, respectively. A list of the domain types and their orientation is reported in Table S1, Supporting Information, together with a quantitative estimation of the relative abundance of each domain.

The transport experiments of this study are carried out on Hall-bar structures patterned by electron beam lithography and consisting of an 8 nm thick *Pt* layer deposited by dc sputtering. Two kinds of devices have been fabricated: large Hall-bars (100 μm long and 20 μm wide), randomly positioned on the sample surface covering multiple structural domains (Figure 1b) and smaller Hall-bars localized at single $CaFe_2O_4$ domains (Figure 1c). In the large devices, the propagation direction of the charge current is oriented parallel to the substrate's $[1\bar{1}0]$ edge. In the small devices, because of the specific requirements dictated by the domains shape, each of the Hall-bars has a slightly unique design but comparable size of approximately 10 μm in length and 3 μm in width. In these devices, the long channel of the Hall-bar and propagation direction of the charge current is parallel to the *b*-axis of the underlying $CaFe_2O_4$ domain. All six different domains were tested in this geometry.

The SMR effect has been measured as the linear, first harmonic response to the applied current (I = 100 to 400 μA, corresponding to a current density J = 0.5 to 4 × 10^5 Acm^{-2}) in transverse and longitudinal geometry using the lock-in detection technique.[33,34] The transverse first-order resistivity, ρ_T^1, normalized over the sheet resistance, ρ_0, is calculated from the measured transverse and longitudinal voltages, V_T and V_L, as:[26]

$$\rho_T^1/\rho_0 = (R_T - R_{0T})/(R_{0L}/g) \quad (1)$$

where $R_T = V_T/I$ and $R_L = V_L/I$ are the transverse and longitudinal resistances, respectively, and R_{0T} and R_{0L} are their respective values without applied magnetic field. $g = l/w$ is a geometric conversion factor given by the ratio of the distance of between longitudinal probes, l, and the width of the Hall-bar, w. Similarly, the normalized longitudinal first-order resistivity ρ_L^1 is given by:

$$\rho_L^1/\rho_0 = (R_L - R_{0L})/(R_{0L}) \quad (2)$$

3. Results

3.1. In-Plane Field Rotation

The dependence of the transverse resistance on the in-plane angle, α, was measured in the large Hall-bars at various temperatures upon heating from 5 K to 300 K. The plot of the ADMR at 7 T for three selected temperatures is shown in **Figure 3**a. In the whole temperature range the measured ADMR can be described with a function of the type:

$$y = y_0 + A_a sin(\alpha + \phi_a)cos(\alpha + \phi_a) + Bsin(\alpha + \phi_{OH}) \quad (3)$$

The first modulation, having a period of 180°, corresponds to the SMR contribution to the transverse resistance. In addition

© 2021 The Authors. Advanced Electronic Materials published by Wiley-VCH GmbH

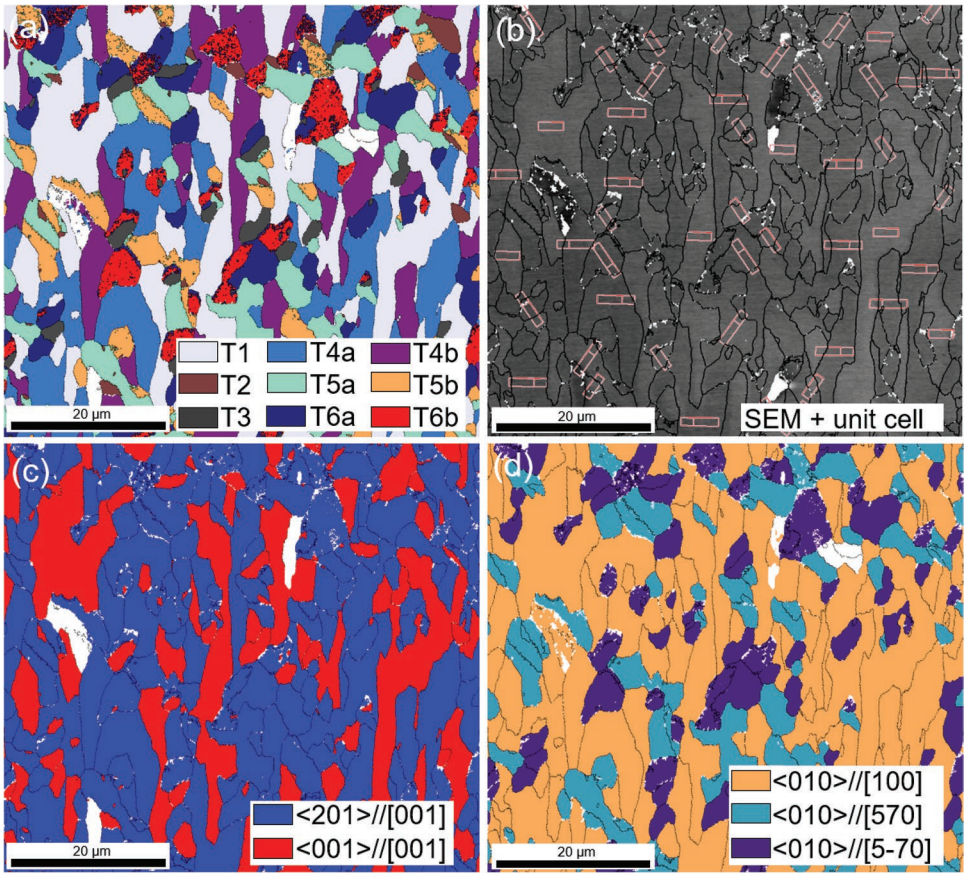

Figure 2. EBSD scan of a 62 μm × 60 μm area of the surface of a 84 nm thick $CaFe_2O_4$ thin film. a) EBSD map showing the nine domain types (solid color). The [100] sample axis (vertical in the presented EBSD map) is parallel to the substrate [1 $\bar{1}$ 0]. b) Map of the SEM secondary electrons contrast with superimposed axonometric projections of the unit cell orientation in red. c) EBSD map highlighting the two different out-of-plane directions: (001) (*T*1-*T*2-*T*3) depicted in red and (302) (*T*4-*T*5-*T*6) in blue. d) EBSD map highlighting the three in-plane directions: domains with the ⟨010⟩ crystal direction parallel to the reference [100] (*T*1-*T*4) are orange, [570] (*T*2-*T*5) are blue and at [5-70] (*T*3-*T*6) are purple. The grain boundaries are indicated with back solid lines in all the maps.

to this, a second component, with period 360° is also present. This is an ordinary Hall effect contribution, caused by an unwanted component of the magnetic field normal to the film surface. An ordinary Hall contribution of 0.127 μΩ at 7 T and 400 μA corresponds to a misalignment of less than 2°, that is plausible given the difficulties to place the sample exactly flat on the holder (this value has been estimated by comparison with the amplitude of the ordinary Hall effect when rotating the magnetic field out-of-plane). The phase of this component and its amplitude, normalized by the carrier concentration, are constant through the whole temperature range, as expected.

Figure 3c shows the temperature dependence of the amplitude (A_a) of the SMR contribution extracted from the fit (see the Supporting Information for a complete account of the fit parameters). The phase ϕ_a is close to 0° in all measurements. At 5 K, the $sin(\alpha)cos(\alpha)$ modulation displays a negative amplitude A_a, corresponding to the typical (negative) SMR response of antiferromagnets.[26,28] Upon increasing temperature, the magnitude of the negative modulation decreases and at about 120 K the SMR effect changes sign, indicating a cross-over from AF to FM or paramagnetic (PM) behavior. Around the zero-crossing point, the value of A_a becomes comparable in magnitude to B, the amplitude of the ordinary Hall effect contribution. Therefore, at this temperature, the shape of the ADMR curve deviates from a 180° periodic modulation, but it is still well-fitted by Equation (3), as shown in Figure 3a. Above 120 K, A_a continues to increase with increasing temperature until 300 K. Surprisingly, no abrupt transition is observed at the the Néel temperature of T_N = 185 K, as observed by means of SQUID magnetometry and Mössbauer spectroscopy in similarly grown samples.[21]

Because the multi-domain nature of the films used in this study adds a further degree of complexity in the interpretation of the ADMR, we turned to measure the six individual $CaFe_2O_4$ structural domains independently (see Section 7). Figure 3b,d shows the dependence of the transverse resistance on the in-plane angle, α, in one of the small Hall-bar devices. The ADMR at 5, 130 and 300 K measured at 200 μA in a field of 7 T is plotted in Figure 3b. As in the case of the larger Hall-bars, the data can be fitted with the model described by Equation (3). However, here A_a is positive across the whole temperature range, indicating the presence of a field-induced magnetic moment dominating over the AF contribution. The amplitude of the SMR contribution, shown in Figure 3d follows a

© 2021 The Authors. Advanced Electronic Materials published by Wiley-VCH GmbH

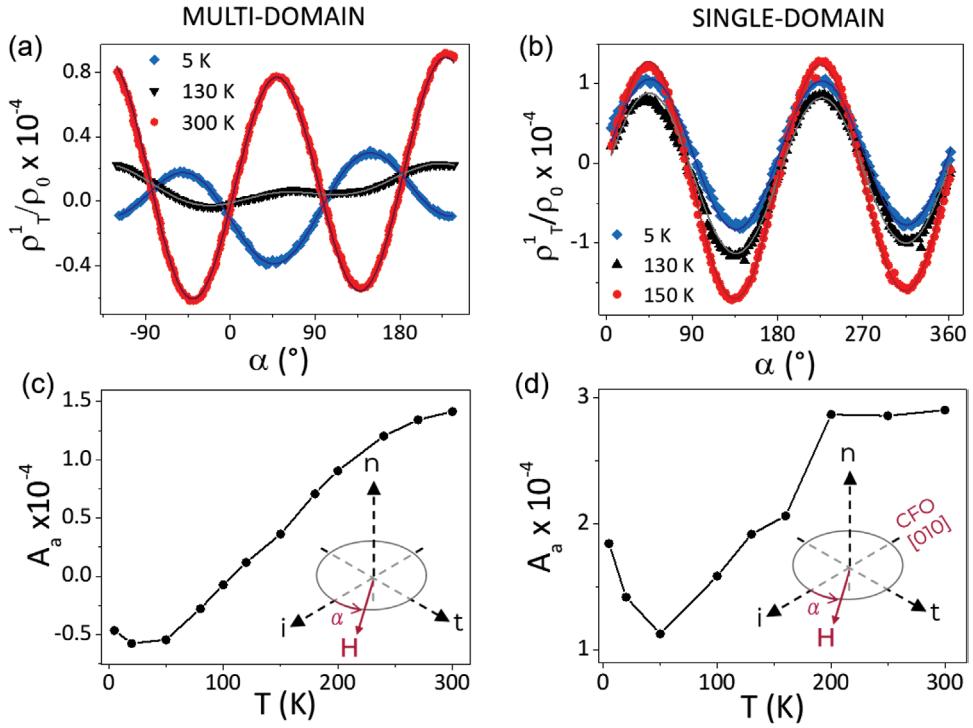

Figure 3. In-plane ADMR of $CaFe_2O_4$ at $H = 7$ T and $J = 2.5$ to 4×10^5 Acm^{-2}. Plot of the normalized first harmonic transverse resistivity, ρ^1_T/ρ_0, as a function of α, together with its fit to Equation (3), at three selected temperatures measured in a large (a) and small (b) Hall-bar device. c,d) Plot of the T dependence of the amplitude, A_a, of the SMR contributions extracted from the fits. In the insets, the geometry of the experiments is indicated, with *i*, *n* and *t* being the directions of the current, interface normal and perpendicular to both of them, respectively. *H* is the applied magnetic field.

non-linear trend with temperature, similar to that observed for the multi-domain bars of Figure 3c: it first decreases between 5 K and 50 K, to then increase between 100 K and 200 K and saturate above T_N. Again, a larger amplitude of the SMR is found above T_N, compared with the value in the ordered sate. At 300 K the magnitude of the SMR effect is comparable to that measured in the easy-plane antiferromagnet NiO[26] and the spin-spiral phase of $CoCr_2O_4$,[33] but lower than the values reported for $\alpha - Fe_2O_3$.[28] However, for an accurate quantitative comparison between these systems the quality of the metal/magnetic insulator interface[1] and *Pt* thickness[35] should also be taken into account.

To exclude that the negative and positive components of the in-plane SMR found in the large devices arise from different structural domains, we have measured individually all the domain types present in the film, as shown in the Supporting Information. Similar sinusoidal modulations of ρ_T and ρ_L, as well as the same field and temperature behaviors, are observed in all cases, regardless of the crystal orientation. This isotropic character of the modulation indicates that the mechanism for the SMR effect in $CaFe_2O_4$ originates on the free rotation of the spin with the applied magnetic field.

In both single- and multi-domain devices, a large positive SMR is observed above the Néel temperature. A non-zero SMR in the paramagnetic state has been measured before in FM (YIG) samples[36] as well as in AF oxides.[33,37] However, its amplitude is expected to decrease following a Curie–Weiss behavior. Here, on the other hand, the amplitude of the modulation above T_N tends to saturate to a fixed value. This is consistent with the non Curie–Weiss susceptibility observed up to 400 K in $CaFe_2O_4$[21,38] and could be explained by the presence of 1D short-range correlations between *Fe* spins found in bulk samples.[38] Below 200 K, the amplitude of the SMR decreases, as the material orders antiferromagnetically. At this temperature however, the amplitude of the modulation is still positive, indicating that the contribution of a net magnetization predominates for applied fields above 1 T. Interestingly, in the multi-domain devices, a cross-over to negative SMR occurs at 120 K, while in the single-domain ones the sign of the modulation is positive at all temperatures. This difference is puzzling as a more intrinsic (AFM-like character) is expected in the single domain devices. The net magnetic moment detected by ADMR is, therefore, not caused by defects uncompensated moments at the boundaries between the different structural domains.

3.2. Out-of-Plane Field Rotation

The ADMR of the large Hall-bar devices was also measured upon rotating the magnetic field outside of the plane of the film. Plots of the longitudinal resistivity, measured at 100 μA in a field of 7 T, as a function of the angles β ($\vec{H}$ rotating within the $n - t$ plane perpendicular to the current direction) and γ ($\vec{H}$ rotating with the $n - i$ plane containing the current direction) are shown in **Figure 4**a,b. In both cases a sinusoidal modulation of the ADMR with period 180° has been observed and the data could be fitted with functions of the type:

© 2021 The Authors. Advanced Electronic Materials published by Wiley-VCH GmbH

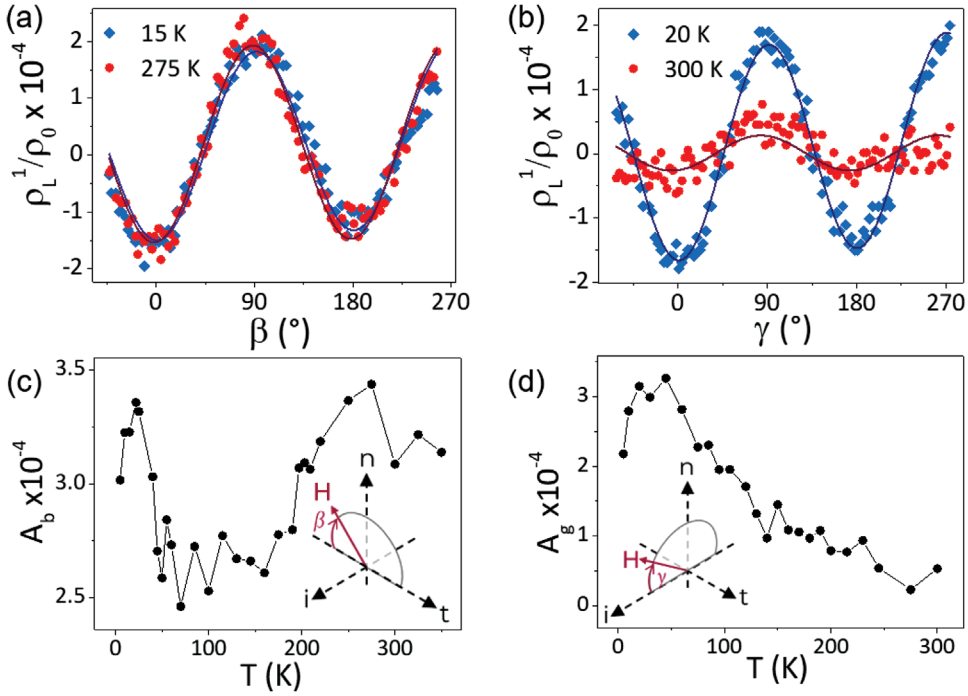

Figure 4. Out-of-plane ADMR of multi-domain $CaFe_2O_4$ at $H = 7$ T and $J = 6.25\ 10^4$ Acm^{-2}. a,b) Plot of the normalized first harmonic longitudinal resistivity, ρ_L^1/ρ_0 as a function of β and γ, respectively, together with their fits to Equations (4) and (5), at two selected temperatures. c,d) Plot of the T dependence of the amplitudes, A_b and A_g, of the SMR contributions extracted from the fits in (a) and (b), respectively. The geometry of the experiments, where n is the direction normal to the plane of the film, i is the direction of the current and t is the in-plane direction perpendicular to i, is shown in the insets.

$$y = y_0 + A_b cos^2(\beta + \phi_b) \quad (4)$$

$$y = y_0 + A_g cos^2(\gamma + \phi_g) \quad (5)$$

where ϕ_b and ϕ_g are close to 90°, indicating that the high resistance state corresponds to the field being perpendicular to the film surface. In addition to the SMR effect, a linear term with time is also added to the fit describing the thermal drifts during the measurement.

Figure 4c,d shows the temperature evolution of the amplitude of the out-of-plane SMR contributions extracted from the fits. As it can be seen, in both plots the sign of the modulation is constant throughout the whole temperature range, while the magnitude of the effect evolves differently with temperature. When the field rotates in the $n - t$ plane (Figure 4a,c), a relatively large SMR is observed at all temperatures between 5 K and 350 K. Here A_b and ϕ_b are almost constant in the whole temperature range. However, when H rotates in the $n - i$ plane (Figure 4b,d) the modulation is largest at low temperatures and decreases significantly upon increasing T. A steeper slope is observed between 50 K and 150 K, that corresponds to the reported ordering of the A magnetic phase, followed by a slower increase until $T_N = 200$ K. Above the T_N and up to 300 K a small modulation is still visible in the data, but the signal size becomes comparable to the noise.

Therefore, the presence of a modulation with both β and γ indicates that both a FM (or PM) component and an AF component contribute to the SMR in the large devices, originating from the rotation of $\vec{M}$ and $\vec{L}$ with the applied field. Combining the temperature evolution of the ADMR of the two out-of-plane geometries yields a similar trend as that observed for the in-plane measurement. This offers further support to the interpretation of the in-plane signal as arising from two components, which now can be isolated in the out-of-plane measurements.

3.3. Field Dependence

The magnetic field dependence of the ADMR has also been investigated and is shown in **Figure 5**. Figure 5a displays a plot of $R_T - R_0$ of a single-domain device as a function of the strength of $\vec{H}$, applied in-plane at $\alpha = 45°$ from the current direction (maximum of the ADMR) at three different temperatures: 5, 100, and 200 K. In all cases an increase of the resistance is found with increasing field with a tendency to saturate above 7 T.

Figure 5b shows a plot of $R_L - R_0$ measured at 100 K in a multi-domain device as a function of the strength of $\vec{H}$, applied in-plane parallel to the current direction (minimum of the ADMR) and out-of-plane (maximum of the ADMR). For a pure antiferromagnet, R_T and R_L scale with H^2. Here, instead, the data is better fitted by a combination of contributions; one with a negative, quadratic increase and one with a positive, linear increase with increasing magnetic field strength, which predominates at lower fields. The latter is observed in paramagnets and indicates the presence of uncoupled spins. The asymmetry between the positive and negative branches of the curves in Figure 5b, is related to the field scan direction (from positive to negative values or vice versa), which can be caused by domain movement and pinning of domain walls.

© 2021 The Authors. Advanced Electronic Materials published by Wiley-VCH GmbH

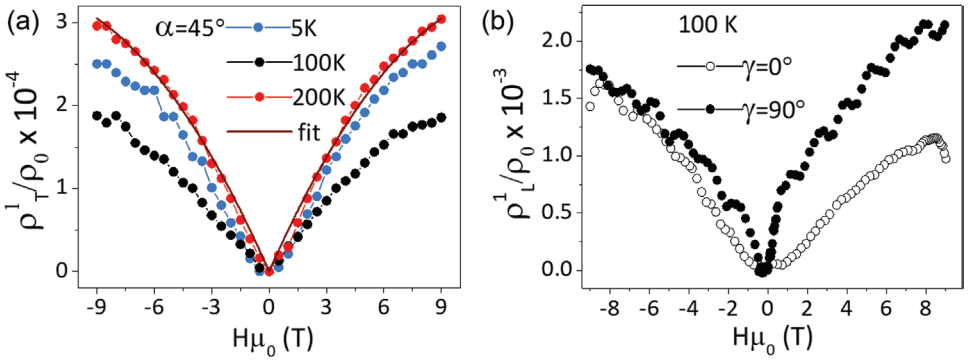

Figure 5. Field dependence of the resistance at a fixed applied field direction. a) Plot of the normalized first harmonic transverse resistivity ρ^1_T/ρ_0 as a function of H measured in a single-domain device at 5 K (blue), 100 K (black) and 200 K (red) for $\alpha = 45°$. The fit of the curve at 200 K with $\rho^1_T/\rho_0 = A|H| - BH^2$ (A, $B > 0$) is also shown in dark red. b) Plot of the normalized first harmonic longitudinal resistivity ρ^1_L/ρ_0 as a function of H measured in a multi-domain device at 100 K for $\gamma = 90°$ (full dots) and $\gamma = 0°$ (open dots).

4. Simulations

In order to improve our understanding of the mechanisms that give rise to a combination of positive and negative SMR in $Pt/CaFe_2O_4$ bilayers, we built a simple theoretical model that simulates the spin configuration of the system and its SMR response in the case in which the Ising condition is lifted. The magnetic properties of an orthorhombic antiferromagnet with uniaxial anisotropy can be described by a Hamiltonian consisting of contributions from Zeeman, exchange, and magnetic anisotropy energies in the form:[3,39]

$$H = -\gamma\hbar\sum_i \vec{H}_0\cdot\vec{S}_i + \sum_{i,j} 2J_{ij}\vec{S}_i\cdot\vec{S}_j - D_y\sum_i (S_i^y)^2 + D_z\sum_i (S_i^z)^2 \quad (6)$$

where $\gamma = g\mu_B/\hbar$ is the gyromagnetic ratio, g the spectroscopic splitting factor, μ_B the Bohr magneton and ħ the reduced Plank constant. $\vec{S}_i$ indicates the spin at a generic lattice site i, $\vec{H}_0$ the applied magnetic field and J_{ij} the exchange constant of the interaction between spins. The system is characterized by two distinct anisotropies, a positive one (hard) with constant D_z along the ⟨001⟩ direction that forces the spins into the $a-b$ plane and a negative (easy) with constant D_y along the magnetic easy axis ⟨010⟩.

$CaFe_2O_4$ has been previously described as a 3D Ising antiferromagnet,[40] where the two antiferromagnetic sublattices are antiparallel to each other and the spins can only display two states, described by two scalar values. In this case, no tilt of the spins is possible under the effect of the magnetic field and, thus, the SMR response should be purely antiferromagnetic (negative amplitude). Therefore, in order to take into account the scenario in which tilting of the spins sublattices is at the origin of the measured positive contribution to the SMR, we utilize in our model a more general Heisenberg Hamiltonian and allow the spins to assume any orientation in space.

In order to find the spin equilibrium configuration, we follow the approach described in ref. [3] and express the energy per unit volume of the system as a function of the angles that the two AF sublattices make with i (easy axis and current direction), θ_1 and θ_2, and with n, φ_1, and φ_2. The coordinates of the energy minima correspond to the equilibrium orientation of the sublattices for different applied magnetic field strengths and directions. The material dependent parameters in the model are the effective exchange, H_E, and anisotropy, H_A, fields defined by:[3,39]

$$H_E = 2SnJ/\gamma\hbar, \qquad H_{Ay} = 2D_yS_i/\gamma\hbar, \qquad H_{Az} = 2D_nS_i/\gamma\hbar \quad (7)$$

where n is the number of nearest neighbors.

For $CaFe_2O_4$ we base our simulations on the values reported in literature for the bulk material: $S = 5/2$ and $g = 2$.[17] The anisotropy constants for $CaFe_2O_4$ have not, to our knowledge, been reported. However indirect measurements have shown an in-plane anisotropy field of 443 Oe at 300 K[38] and a resonance field along the c-axis of 3380 Oe. The theoretically predicted AF exchange constants are $J_1 = -4.19$ K, $J_2 = -5.44$ K, $J_3 = -14.69$ K and $J_4 = -23.93$ K.[16] Thus, the negative inter-chain J_3 and J_4 are the dominant inter-sublattice interactions. Therefore, for simplification, we can consider one unique exchange interaction with magnitude mean between J_3 and J_4 and number of nearest neighbors $n = 4$, corresponding to the adjacent Fe^{3+} spins connected through corner-sharing O_6 octahedra. This leads to a calculated H_E of 287 T, that is lower than what is reported for the easy-plane antiferromagnet NiO, but higher than the easy-axis MnF_2 and FeF_2.[3] The corresponding spin-flop field would be $H_{SF} = \sqrt{2H_AH_E} = 5$ T. Using this set of parameters, where H_E is two orders of magnitude larger than the applied H_0 and H_{Ay} much smaller, the expected SMR response, shown in **Figure 6**, is governed by the AF exchange and differs largely from what is observed experimentally in all 3 planes of rotation.

In fact, when a 7 T field is applied along the magnetic easy axis, the simulation of the equilibrium position of the AF sublattices shows that the two sublattices align antiferromagnetically in the direction perpendicular to the applied field (spin-flop state) with $\theta_1 = \varphi_1 = \varphi_2 = 90°$ and $\theta_2 = -90°$, as observed in Figure 6a,b. Rotating the magnetic field in the $i-t$ plane produces a coherent rotation of θ_1 and θ_2 with α which leads to a sinusoidal modulation of the SMR effect with negative amplitude. Increasing the strength of the magnetic field increases the amplitude of the modulation, as shown in Figure 6c up to 9 T. On the contrary, when H is below the spin-flop value of about 5 T, the modulation deviates from sinusoidal, as the sublattices

© 2021 The Authors. Advanced Electronic Materials published by Wiley-VCH GmbH

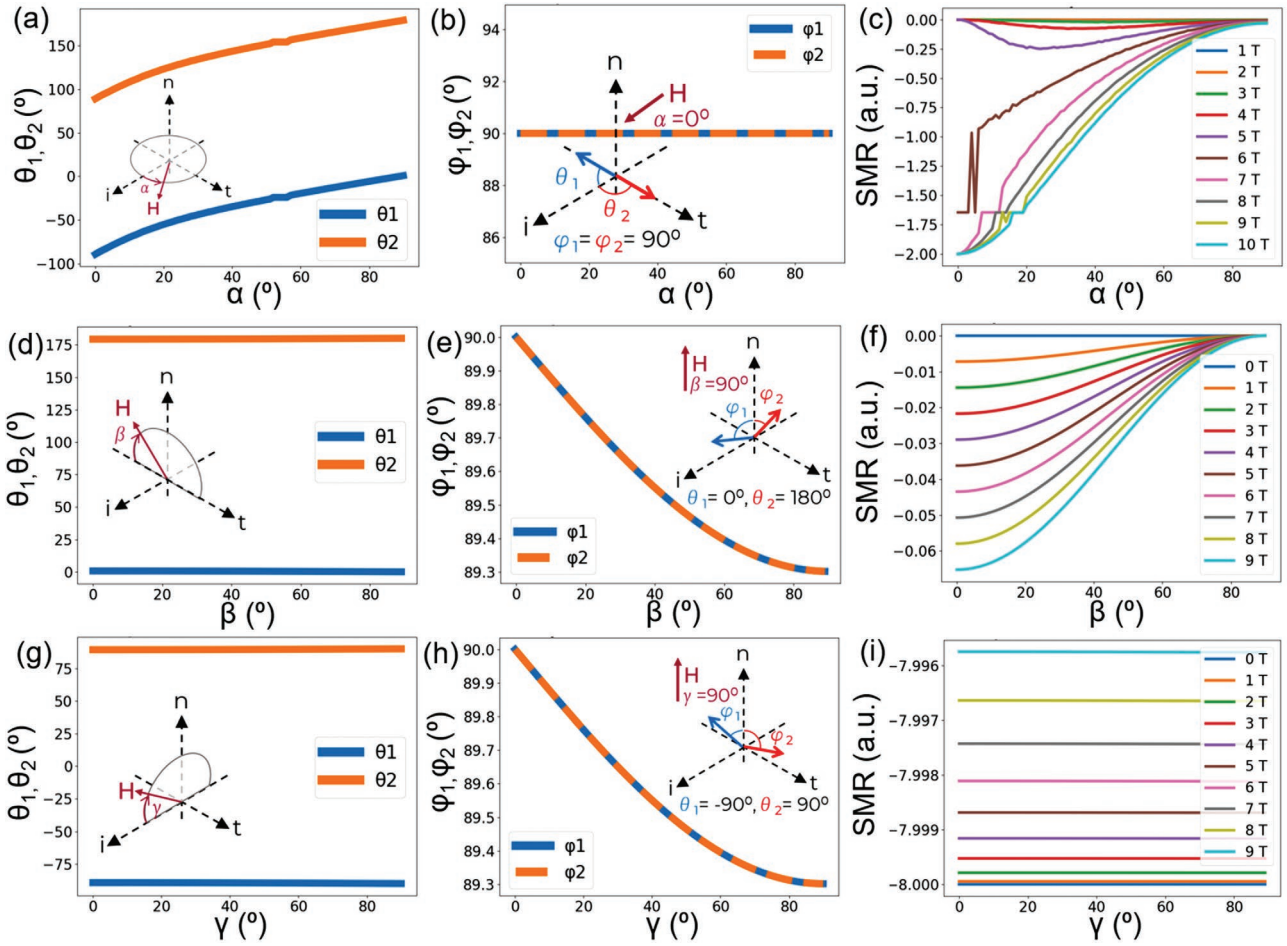

Figure 6. Simulation of the sublattices equilibrium positions for He = 287 T, H_{Ay} = 0.044 T, H_{Az} = 0.338 T and H_0 = 7 T. Plot of a) θ_1 and θ_2, b) φ_1 and φ_2 and c) field-dependent longitudinal SMR as a function of α when the field rotates in the (easy) $i-t$ plane. Plot of d) θ_1 and θ_2, e) φ_1 and φ_2 and f) field-dependent longitudinal SMR as a function of β when the field rotates in the $t-n$ plane. Plot of g) θ_1 and θ_2, h) φ_1 and φ_2 and i) field-dependent longitudinal SMR as a function of γ when the field rotates in the $i-n$ plane. Sketches of the rotation geometry and of the two AF sublattices (as blue and red arrows) are shown in the inset for fields angles of 0° and 90°.

only slightly rotate around the equilibrium configuration with $\theta_1 = 0°$ and $\theta_2 = 180°$

When the applied field rotates outside of the film plane, in addition to the in-plane rotation, the sublattices also start to tilt out-of-plane (Figure 6e,h), but the tilt is limited to a few degrees. When $\beta = 90°$ and $\gamma = 90°$, corresponding to the same out-of-plane field orientation, the in-plane configuration of the two sublattices is not identical: in the first case (Figure 6e) the spins align along the easy axis ($\theta_1 = 0°$, $\theta_2 = 180°$), as expected, while in the second case (Figure 6h) they are perpendicular ($\theta_1 = -90°$, $\theta_2 = 90°$). This is due to the small value of H_{Ay}, that makes the energy minima of these two configurations very close to each other. As a result, a very small modulation (compared to the in-plane modulation) is observed in the β scan, in contradiction with our experiments. A modulation in this direction is instead typical of ferromagnets or paramagnets. In addition, no modulation in the γ scan is expected from the simulations (Figure 6i). Again this is different from what is observed experimentally (Figure 4b), where a modulation with maximum at $\gamma = 90°$ is found. Assuming a larger H_{Ay} value, that could be plausible given the shape anisotropy of the needle-like crystals, the configuration with $\gamma = 90°$, $\theta_1 = 0°$ and $\theta_2 = 180°$ would be energetically favored, resulting in a rotation of the sublattices in the $i-t$ plane. This can lead to an ADMR with maximum at $\gamma = 90°$, as observed experimentally. However, in this case the amplitude of the SMR would decrease with increasing applied field, as the sublattices tilt towards the easy axis from the spin-flop configuration at $\gamma = 0°$, raising the value of the low resistance state. This is also inconsistent with our experimental measurements, that show a slight increase of the out-of-plane modulation with increasing applied field (see Supporting Information).

5. Discussion

From these simulations, it is evident that the positive SMR response measured experimentally cannot be explained by the spin canting of a uniaxial antiferromagnet with exchange and anisotropy field values as reported in literature for $CaFe_2O_4$. For the external magnetic field to be able to induce a large enough canting of the AF sublattices in the spin-flop state that results

© 2021 The Authors. Advanced Electronic Materials published by Wiley-VCH GmbH

in a positive SMR amplitude, its value has to be comparable to H_E. However, this cannot be the case for $CaFe_2O_4$ films, given the T_N of 185 K. In addition, even in a scenario with lower H_E, the model would not completely capture the measured behavior in the field-dependence of the SMR and in the field rotation in the $n-i$ plane. Therefore, it is clear that the observed positive contribution to the SMR cannot be intrinsic to the AF ordering, arising from a tilt of the sublattices with the magnetic field, and instead a different source for such positive contribution needs to be taken into account to explain the observed ADMR.

One possibility is that the material displays additional spins that are not accounted for in our theoretical model. This would be in good agreement with the observed opening of the $M-H$ loops at around 130 K in both bulk[17] and thin films,[21] which is proposed to originate from "orphan spins" at the magnetic antiphase boundaries.[19,40] In addition, short-range 1D interactions and up to 350 K[16] and a even higher Curie–Weiss temperature[40] have been reported in $CaFe_2O_4$ single crystals and could also explain the persistence of the orphan spins signal at temperatures above T_N.

Another possible origin for this positive contribution would be surface and shape effects.[41] It is well-known,[42–44] that due to surface magnetic anisotropy and magneto-elastic strain at the surface, the magnetic structure of the the top few nm can largely differ from that of bulk. These become particularly relevant in AF nanoparticles, even up to 500 nm in size, due to the finite-size and shape constraints. For example, loss of long-range ordering or another type of structure or a change of easy axis can occur at the surface,[45] as well as different reorientation behaviour with an applied magnetic field.[46] In our case, due to the needle-shape of the crystals with large aspect ratio and a width in the 100 nm range, these effects may play an important role. To include such effects in the SMR model, a much more complex approach to the simulation of the spin structure of $CaFe_2O_4$ thin films, beyond the scope of this paper, is required.

We also considered, but excluded, that the positive modulation arises from effects other than the SMR. In particular, the Hanle magnetoresistance, originating from the precession of edge spin accumulation,[47,48] is a common source of artifacts in SMR measurements as it is also characterized by a resistance modulation with period 180° and a phase similar to positive SMR. The modulation induced by the Hanle effect is analogous to the SMR response of a FM and only appears when the field rotates in the $i-t$ and $n-t$ planes. In order to distinguish between the contributions from the Hanle and SMR effects, the field dependence resistance can be studied for a fixed direction of the applied field, as shown in Figure 5. For the Hanle effect, a positive quadratic increase of R_L and R_T with $\vec{H}$ is expected, and this differs from what is measured for both small and large devices, where a linear increase at low fields and a quadratic negative saturation at higher fields always occurs. In addition, a modulation arising from this effect would show a monotonic trend with temperature, which is different from our observations in both single- and multi-domain devices.

Anisotropic magnetoresistance arising from the magnetic proximity effects has also been observed in FM/Pt bilayers, that can compromise the use of thin Pt as a detector of pure spin current.[49,50] However, the magnitude of this effect is expected to be much lower in compensated antiferromagnets where a net magnetization can only appear locally due to uncompensated domain boundaries.[50] This effect is known to induce a ADMR when $\vec{H}$ rotates in the $n-i$ plane and, thus, cannot explain the positive modulation observed in the β scan.[4,51]

Therefore, we believe that the most likely explanation for the observed ADMR is the SMR effect arising from the rotation of the Néel vector of the AF structure and an additional positive contribution that originates from uncompensated spins at the antiphase boundaries. These spins, which do not generally interact with each other, will give rise to a linear, paramagnetic-like, field-induced magnetization but they will, generally, not order at a finite temperature, as it is observed in $CaFe_2O_4$. However, interactions between orphan spins could emerge thanks to the large correlation lengths that develop around the second-order antiferromagnetic phase transition.[21] This would explain the appearance of a net magnetization in a limited temperature range. However, the possibility of surface effects due to the small size of the crystals composing the films cannot be excluded.

6. Conclusions

We have measured the ADMR in $Pt/CaFe_2O_4$ bilayers for both multi and single structural domain devices. The sinusoidal modulation of the Pt resistance for both in-plane and out-of-plane field rotations and the magnetic field dependence indicate the presence of two contributions to the SMR: a negative and a positive one. The former depends quadratically on the magnetic field and its intensity decreases with increasing temperature, corresponding to the rotation of the Néel vector of the antiferromagnetic ordering. The latter depends linearly on the magnetic field, occurs at all temperatures and is consistent with the presence of uncompensated spins that are uncoupled from the AF ordering. These observations support the scenario in which spin fluctuations create antiphase boundaries in the B phase ($\uparrow\downarrow\uparrow\downarrow$ ground state), that locally display $\uparrow\uparrow\downarrow\downarrow$ spin ordering characteristic of the A-phase. At the antiphase boundaries, uncompensated moments, that are free to rotate with the applied magnetic field, are present, leading to a positive contribution to the SMR. We hypothesize that, in the proximity of the critical phase transition, when long-range correlations emerge, the coherent effect of these antiphase boundaries gives rise to the observed net magnetic moment. Finally, additional effects from confinement and anisotropy at the surface cannot be ruled out, and they could play a role in the difference between the behaviour of single and multi-domain devices. Although such a difference is not fully explained yet, the experiments show the potential of multiscale SMR measurements to extract unique information from complex magnetic samples.

7. Experimental Section

Device Fabrication: Both large and small Hall-bars were fabricated by means of the e-beam lithography. In the first stage, *Au* markers were deposited on the sample by means of DC sputtering through polymethylmethacrylate (PMMA) shadow mask. PMMA masks were prepared on a separate substrate and later placed on top of the sample with alignment done under the optical microscope. After deposition,

© 2021 The Authors. Advanced Electronic Materials published by Wiley-VCH GmbH

the masks were removed mechanically without dissolving PMMA. This methodology assures that sample surface at all stages of the fabrication process is never in contact with PMMA dissolved in solution. This considerably reduces the amount of polymer residues typically present after conventional fabrication methods. Further details of the preparation of the PMMA shadow masks will be provided in a separate publication. In the second stage, 8 nm of platinum were sputtered in a shape of the Hall-bar (either large or small) again using PMMA shadow masks in order to ensure minimal level of contamination of the interface between *Pt* and $CaFe_2O_4$. In the last step, via conventional PMMA-based e-beam lithography, the arms of the Hall-bars were connected with *Ti*/*Au* (5 nm/55 nm) contacts which were later on bonded with *Al* wires to the chip carrier of the used measurement setup.

Electrical Measurements: The SMR effect has been measured using the lock-in detection technique[33] in transverse and longitudinal geometry. Using multiple Stanford Research SR-830 lock-in amplifiers the first and second harmonic voltage responses (V_1 and V_2) were recorded simultaneously. The input AC current (I_0) was a sine wave with frequency of 17 Hz and amplitude of 100–200 μA for the small devices and 100–400 μA for the large ones, generated by a Stanford Research System Model CS580 Voltage Controlled Current Source. The ADMR of the *Pt* was measured by rotating the sample in a magnetic field, with α being the angle between the current direction and $\vec{H}$, when $\vec{H}$ rotates in the plane of the film and β and γ being the out-of-plane angles. The response was measured at different T and $\vec{H}$ in a Quantum Design Physical Properties Measurement System (PPMS).

Simulations: The simulations of the sublattices equilibrium positions and SMR effect were performed using a simple code written in python. The code utilizes the scipy.minimize package for a numerical minimization of the energy as a function of θ_1, θ_2, φ_1, and φ_2 for a given set of parameters H_E, H_{Ay}, H_{Az}, and H_0. The process is repeated for different values of the applied field direction.

Considering a single domain with $\vec{H}_0$ rotating in the film plane, the energy is given by:

$$\begin{aligned} E/M = &-H_0 cos(\alpha)[cos(\theta_1)sin(\varphi_1)+cos(\theta_2)sin(\varphi_2)] \\ &-H_0 sin(\alpha)[sin(\theta_1)sin(\varphi_1)+sin(\theta_2)sin(\varphi_2)] \\ &+H_E[sin(\varphi_1)sin(\varphi_2)cos(\theta_1-\theta_2)+cos(\varphi_1)cos(\varphi_2)] \\ &-H_{Ay}[cos^2(\theta_1)sin^2(\varphi_1)+cos^2(\theta_2)sin^2(\varphi_2)]+H_{Az}[cos^2(\varphi_1)+cos^2(\varphi_2)] \end{aligned} \quad (8)$$

where α is the angle between $\vec{H}_0$ and the easy axis *b*.

Similar expressions have been used to model the response when the field is rotated outside of the film plane. To simulate the response of the different domains, the relative in-plane and out-of-plane tilts from the *b* and *c*-axis have also been taken into account.

The magnetization and Néel vectors were then calculated as sum and difference of the vectors describing the position of the two AF sublattices at the energy minimum. Finally the FM and AF contributions to the SMR were calculated as the negative squared dot product between the relative order parameter vector and the spin accumulation direction at the interface. Because the modulus of each sublattice vector is arbitrarily set equal to 1 and the amplitude of the spin accumulation is not known, the model does not provide a quantitative measure of the magnitude of the SMR effect.

Supporting Information

Supporting Information is available from the Wiley Online Library or from the author.

Acknowledgements

The authors are grateful to Prof. Dr. Thom Palstra, Prof. Dr. Maxim Mostovoy, Dr. Maria Azhar, Dr. Aisha Aqeel, Dr. Arijit Das and Frank Feringa for the useful scientific discussions and insight in the interpretation of the experimental data. S.D. also gratefully acknowledges the technical support of Jacob Baas in performing the experiments of this study. Financial support by the Groningen Cognitive Systems and Materials Center (CogniGron) and the Ubbo Emmius Funds of the University of Groningen is gratefully acknowledged.

Conflict of Interest

The authors declare no conflict of interest.

Data Availability Statement

The data that support the findings of this study is available in the open access repository DataverseNL at https://doi.org/10.34894/N8WDHW.

Keywords

antiferromagnet, domains, spin Hall magnetoresistance

Received: September 8, 2021
Revised: November 18, 2021
Published online: December 17, 2021

[1] A. Mahmood, W. Echtenkamp, M. Street, J.-L. Wang, S. Cao, T. Komesu, P. A. Dowben, P. Buragohain, H. Lu, A. Gruverman, A. Parthasarathy, S. Rakheja, C. Binek, *Nat. Commun.* **2021**, *12*, 1674.
[2] T. Jungwirth, X. Marti, P. Wadley, J. Wunderlich, *Nat. Nanotechnol.* **2016**, *11*, 231.
[3] S. M. Rezende, A. Azevedo, R. L. Rodríguez-Suárez, *J. Appl. Phys.* **2019**, *126*, 151101.
[4] Y. Luo, C. Liu, H. Saglam, Y. Li, W. Zhang, S. S.-L. Zhang, J. E. Pearson, B. Fisher, T. Zhou, A. Bhattacharya, A. Hoffmann, *Phys. Rev. B* **2021**, *103*, L020401.
[5] T. Moriyama, K. Oda, T. Ohkochi, M. Kimata, T. Ono, *Sci. Rep.* **2018**, *8*, 14167.
[6] C. O. Avci, A. Quindeau, C.-F. Pai, M. Mann, L. Caretta, A. S. Tang, M. C. Onbasli, C. A. Ross, G. S. Beach, *Nat. Mater.* **2017**, *16*, 309.
[7] O. J. Amin, K. W. Edmonds, P. Wadley, *Appl. Phys. Lett.* **2020**, *117*, 010501.
[8] T. Hajiri, S. Ishino, K. Matsuura, H. Asano, *Appl. Phys. Lett.* **2019**, *115*, 052403.
[9] Y.-T. Chen, S. Takahashi, H. Nakayama, M. Althammer, S. T. B. Goennenwein, E. Saitoh, G. E. W. Bauer, *Phys. Rev. B* **2013**, *87*, 144411.
[10] G. R. Hoogeboom, T. Kuschel, G. E. Bauer, M. V. Mostovoy, A. V. Kimel, B. J. van Wees, *Phys. Rev. B* **2021**, *103*, 134406.
[11] S. Becker, A. Ross, R. Lebrun, L. Baldrati, S. Ding, F. Schreiber, F. Maccherozzi, D. Backes, M. Kläui, G. Jakob, *Phys. Rev. B* **2021**, *103*, 24423.
[12] T. Hajiri, L. Baldrati, R. Lebrun, M. Filianina, A. Ross, N. Tanahashi, M. Kuroda, W. L. Gan, T. O. Menteş, F. Genuzio, A. Locatelli, H. Asano, M. Kläui, *J. Phys.: Condens. Matter* **2019**, *31*, 445804.
[13] Y. Ji, J. Miao, K. K. Meng, X. G. Xu, J. K. Chen, Y. Wu, Y. Jiang, *Jpn. J. Appl. Phys.* **2019**, *58*, 060911.
[14] H. Wang, D. Hou, Z. Qiu, T. Kikkawa, E. Saitoh, X. Jin, *J. Appl. Phys.* **2017**, *122*, 083907.
[15] A. Aqeel, N. Vlietstra, A. Roy, M. Mostovoy, B. J. Van Wees, T. T. M. Palstra, *Phys. Rev. B* **2016**, *94*, 134418.
[16] R. Das, S. Debnath, G. N. Rao, S. Narasimhan, F. C. Chou, *Phys. Rev. B* **2018**, *98*, 144404.

© 2021 The Authors. Advanced Electronic Materials published by Wiley-VCH GmbH

[17] C. Stock, E. E. Rodriguez, N. Lee, M. A. Green, F. Demmel, R. A. Ewings, P. Fouquet, M. Laver, C. Niedermayer, Y. Su, K. Nemkovski, J. A. Rodriguez-Rivera, S. W. Cheong, *Phys. Rev. Lett.* **2016**, *117*, 017201.
[18] H. Watanabe, H. Yamauchi, M. Ohashi, M. Sugimoto, T. Okada, M. Fukase, *J. Phys. Soc. Jpn.* **1967**, *22*, 939.
[19] C. Stock, E. E. Rodriguez, N. Lee, F. Demmel, P. Fouquet, M. Laver, C. Niedermayer, Y. Su, K. Nemkovski, M. A. Green, J. A. Rodriguez-Rivera, J. W. Kim, L. Zhang, S. W. Cheong, *Phys. Rev. Lett.* **2017**, *119*, 257204.
[20] M. Songvilay, S. Petit, M. Koza, S. Rols, E. Suard, V. Skumryev, C. Martin, F. Damay, *Phys. Rev. B* **2020**, *101*, 014407.
[21] S. Damerio, P. Nukala, J. Juraszek, P. Reith, H. Hilgenkamp, B. Noheda, *npj Quantum Mater.* **2020**, *5*, 33.
[22] H. Lane, E. E. Rodriguez, H. C. Walker, C. Niedermayer, U. Stuhr, R. I. Bewley, D. J. Voneshen, M. A. Green, J. A. Rodriguez-Rivera, P. Fouquet, S.-W. Cheong, J. P. Attfield, R. A. Ewings, C. Stock, *Phys. Rev. B* **2021**, *104*, 104404.
[23] Z. Z. Luan, F. F. Chang, P. Wang, L. F. Zhou, J. F. K. Cooper, C. J. Kinane, S. Langridge, J. W. Cai, J. Du, T. Zhu, D. Wu, *Appl. Phys. Lett.* **2018**, *113*, 072406.
[24] S. Geprägs, M. Opel, J. Fischer, O. Gomonay, P. Schwenke, M. Althammer, H. Huebl, R. Gross, *J. Appl. Phys.* **2020**, *127*, 243902.
[25] L. Baldrati, A. Ross, T. Niizeki, C. Schneider, R. Ramos, J. Cramer, O. Gomonay, M. Filianina, T. Savchenko, D. Heinze, A. Kleibert, E. Saitoh, J. Sinova, M. Kläui, *Phys. Rev. B* **2018**, *98*, 024422.
[26] G. R. Hoogeboom, A. Aqeel, T. Kuschel, T. T. M. Palstra, B. J. Van Wees, *Appl. Phys. Lett.* **2017**, *111*, 052409.
[27] J. Fischer, O. Gomonay, R. Schlitz, K. Ganzhorn, N. Vlietstra, M. Althammer, H. Huebl, M. Opel, R. Gross, S. T. B. Goennenwein, S. Geprägs, *Phys. Rev. B* **2018**, *97*, 014417.
[28] J. Fischer, M. Althammer, N. Vlietstra, H. Huebl, S. T. Goennenwein, R. Gross, S. Geprägs, M. Opel, *Phys. Rev. Appl.* **2020**, *13*, 014019.
[29] C. O. Avci, *J. Phys. Soc. Jpn.* **2021**, *90*, 081007.
[30] P. Wang, H. Zhao, Z. Luan, S. Xia, T. Feng, L. Zhou, *Chin. Phys. B* **2021**, *30*, 027510.
[31] B.-W. Dong, J. Cramer, K. Ganzhorn, H. Y. Yuan, E.-J. Guo, S. T. B. Goennenwein, M. Kläui, *J. Phys.: Condens. Matter* **2017**, *30*, 035802.
[32] K. Ganzhorn, J. Barker, R. Schlitz, B. A. Piot, K. Ollefs, F. Guillou, F. Wilhelm, A. Rogalev, M. Opel, M. Althammer, S. Geprägs, H. Huebl, R. Gross, G. E. W. Bauer, S. T. B. Goennenwein, *Phys. Rev. B* **2016**, *94*, 094401.
[33] A. Aqeel, N. Vlietstra, J. A. Heuver, G. E. W. Bauer, B. Noheda, B. J. van Wees, T. T. M. Palstra, *Phys. Rev. B* **2015**, *92*, 224410.
[34] N. Vlietstra, J. Shan, B. Van Wees, M. Isasa, F. Casanova, J. B. Youssef, *Phys. Rev. B* **2014**, *90*, 174436.
[35] N. Vlietstra, J. Shan, V. Castel, B. Van Wees, J. B. Youssef, *Phys. Rev. B* **2013**, *87*, 184421.
[36] M. Lammel, R. Schlitz, K. Geishendorf, D. Makarov, T. Kosub, S. Fabretti, H. Reichlova, R. Huebner, K. Nielsch, A. Thomas, S. T. B. Goennenwein, *Appl. Phys. Lett.* **2019**, *114*, 252402.
[37] R. Schlitz, T. Kosub, A. Thomas, S. Fabretti, K. Nielsch, D. Makarov, S. T. B. Goennenwein, *Appl. Phys. Lett.* **2018**, *112*, 132401.
[38] A. C. Gandhi, R. Das, F.-C. Chou, J. G. Lin, *J. Phys.: Condens. Matter* **2017**, *29*, 175802.
[39] F. L. A. Machado, P. R. T. Ribeiro, J. Holanda, R. L. Rodríguez-Suárez, A. Azevedo, S. M. Rezende, *Phys. Rev. B* **2017**, *95*, 104418.
[40] H. Lane, C. Stock, S.-W. Cheong, F. Demmel, R. Ewings, F. Krüger, *Phys. Rev. B* **2020**, *102*, 024437.
[41] Y. Ji, J. Miao, Y. M. Zhu, K. K. Meng, X. G. Xu, J. K. Chen, Y. Wu, Y. Jiang, *Appl. Phys. Lett.* **2018**, *112*, 232404.
[42] H. Gomonay, V. M. Loktev, *J. Phys.: Condens. Matter* **2002**, *14*, 3959.
[43] O. Gomonay, S. Kondovych, V. Loktev, *J. Magn. Magn. Mater.* **2014**, *354*, 125.
[44] L. D. Landau, E. M. Lifshitz, *Theory of Elasticity*, Elsevier, Amsterdam **2013**.
[45] D. Tobia, E. Winkler, R. Zysler, M. Granada, H. Troiani, *Phys. Rev. B* **2008**, *78*, 104412.
[46] A. N. Bogdanov, A. V. Zhuravlev, U. K. Rößler, *Phys. Rev. B* **2007**, *75*, 094425.
[47] H. Wu, X. Zhang, C. H. Wan, B. S. Tao, L. Huang, W. J. Kong, X. F. Han, *Phys. Rev. B* **2016**, *94*, 174407.
[48] S. Vélez, V. N. Golovach, A. Bedoya-Pinto, M. Isasa, E. Sagasta, M. Abadia, C. Rogero, L. E. Hueso, F. S. Bergeret, F. Casanova, *Phys. Rev. Lett.* **2016**, *116*, 016603.
[49] S.-Y. Huang, X. Fan, D. Qu, Y. P. Chen, W. G. Wang, J. Wu, T. Y. Chen, J. Q. Xiao, C. L. Chien, *Phys. Rev. Lett.* **2012**, *109*, 107204.
[50] S. Geprägs, S. Meyer, S. Altmannshofer, M. Opel, F. Wilhelm, A. Rogalev, R. Gross, S. T. Goennenwein, *Appl. Phys. Lett.* **2012**, *101*, 262407.
[51] M. Gamino, D. S. Maior, L. H. Vilela-Leão, R. L. Rodríguez-Suárez, F. L. A. Machado, A. Azevedo, S. M. Rezende, *J. Magn. Magn. Mater.* **2019**, *475*, 586.

© 2021 The Authors. Advanced Electronic Materials published by Wiley-VCH GmbH